

# LIMITS ON THE ULTRA-BRIGHT FAST RADIO BURST POPULATION FROM THE CHIME PATHFINDER

CHIME SCIENTIFIC COLLABORATION,<sup>1</sup> M. AMIRI,<sup>2</sup> K. BANDURA,<sup>3,4</sup> P. BERGER,<sup>5,6</sup> J. R. BOND,<sup>7,5</sup> J.F. CLICHE,<sup>8</sup> L. CONNOR,<sup>9,10</sup> M. DENG,<sup>2</sup> N. DENMAN,<sup>11,12</sup> M. DOBBS,<sup>8,7</sup> R.S. DOMAGALSKI,<sup>12,6</sup> M. FANDINO,<sup>2</sup> A.J. GILBERT,<sup>8</sup> D.C. GOOD,<sup>2</sup> M. HALPERN,<sup>2,7</sup> D. HANNA,<sup>8</sup> A.D. HINCKS,<sup>2,13</sup> G. HINSHAW,<sup>2,7</sup> C. HÖFER,<sup>2</sup> G. HSYU,<sup>14</sup> P. KLAGES,<sup>12,15</sup> T.L. LANDECKER,<sup>16</sup> K. MASUI,<sup>2</sup> J. MENA-PARRA,<sup>14</sup> L.B. NEWBURGH,<sup>17</sup> N. OPPERMAN,<sup>5,12</sup> U.L. PEN,<sup>5,7,18,12</sup> J.B. PETERSON,<sup>19,12</sup> T. PINSONNEAULT-MAROTTE,<sup>2</sup> A. RENARD,<sup>12</sup> J.R. SHAW,<sup>2</sup> S.R. SIEGEL,<sup>8</sup> K. SMITH,<sup>18</sup> E. STORER,<sup>8</sup> I. TRETYAKOV,<sup>12,6</sup> K. VANDERLINDE,<sup>12,6</sup> AND D.V. WIEBE<sup>2</sup>

<sup>1</sup>The Canadian Hydrogen Intensity Mapping Experiment, DRAO, Kaledan B.C., V0H 1k0

<sup>2</sup>Department of Physics and Astronomy, the University of British Columbia

<sup>3</sup>LCSEE, West Virginia University, Morgantown, WV 26505, USA

<sup>4</sup>Center for Gravitational Waves and Cosmology, West Virginia University, Chestnut Ridge Research Building, Morgantown, WV 26505, USA

<sup>5</sup>Canadian Institute for Theoretical Astrophysics, 60 St. George St., Toronto, ON, M5S 3H8, Canada

<sup>6</sup>Department of Physics, University of Toronto, 60 St George St, Toronto, ON, M5S 3H4, Canada

<sup>7</sup>Canadian Institute for Advanced Research, Toronto, ON, Canada, M5G 1Z8

<sup>8</sup>Department of Physics, McGill University, Montreal, Quebec H3A 2T8, Canada

<sup>9</sup>ASTRON, Netherlands Institute for Radio Astronomy, Postbus 2, 7990 AA Dwingeloo, The Netherlands

<sup>10</sup>Anton Pannekoek Institute for Astronomy, University of Amsterdam, Science Park 904, 1098 XH Amsterdam, The Netherlands

<sup>11</sup>Department of Astronomy, the University of Toronto

<sup>12</sup>Dunlap Institute for Astronomy & Astrophysics, 50 St. George St., Toronto, ON, M5S 3H4, Canada

<sup>13</sup>Department of Physics, University of Rome “La Sapienza”, Piazzale Aldo Moro 5, I-00185 Rome, Italy

<sup>14</sup>Department of Physics, McGill University, 3600 University St., Montreal, QC H3A 2T8, Canada

<sup>15</sup>Department of Radiation Oncology, University of Texas Southwestern Medical Center, Dallas, TX 75390

<sup>16</sup>Dominion Radio Astrophysical Observatory, Herzberg Program in Astronomy and Astrophysics, National Research Council Canada

<sup>17</sup>Department of Physics, Yale University, New Haven, CT 06520

<sup>18</sup>Perimeter Institute for Theoretical Physics, Waterloo, ON N2L 2Y5, Canada

<sup>19</sup>McWilliams Center for Cosmology, Dept. of Physics, Carnegie Mellon University, 5000 Forbes Ave, Pittsburgh, PA 15208, USA

## ABSTRACT

We present results from a new incoherent-beam Fast Radio Burst (FRB) search on the Canadian Hydrogen Intensity Mapping Experiment (CHIME) Pathfinder. Its large instantaneous field of view (FoV) and relative thermal insensitivity allow us to probe the ultra-bright tail of the FRB distribution, and to test a recent claim that this distribution’s slope,  $\alpha \equiv -\frac{\partial \log N}{\partial \log S}$ , is quite small. A 256-input incoherent beamformer was deployed on the CHIME Pathfinder for this purpose. If the FRB distribution were described by a single power-law with  $\alpha = 0.7$ , we would expect an FRB detection every few days, making this the fastest survey on sky at present. We collected 1268 hours of data, amounting to one of the largest exposures of any FRB survey, with over  $2.4 \times 10^5 \text{ deg}^2 \text{ hrs}$ . Having seen no bursts, we have constrained the rate of extremely bright events to  $< 13 \text{ sky}^{-1} \text{ day}^{-1}$  above  $\sim 220 \sqrt{(\tau/\text{ms})} \text{ Jy ms}$  for  $\tau$  between 1.3 and 100 ms, at 400–800 MHz. The non-detection also allows us to rule out  $\alpha \lesssim 0.9$  with 95% confidence, after marginalizing over uncertainties in the GBT rate at 700–900 MHz, though we show that for a cosmological population and a large dynamic range in flux density,  $\alpha$  is brightness-dependent. Since FRBs now extend to large enough distances that non-Euclidean effects are significant, there is still expected to be a dearth of faint events and relative excess of bright events. Nevertheless we have constrained the allowed number of ultra-intense FRBs. While this does not

have significant implications for deeper, large-FoV surveys like full CHIME and APERTIF, it does have important consequences for other wide-field, small dish experiments.

## 1. INTRODUCTION

Fast radio bursts (FRBs) are extragalactic, millisecond radio transients, of which roughly two dozen have been reported (Lorimer et al. 2007; Thornton et al. 2013; Petroff et al. 2015a). Though the exact origin of FRBs remains elusive, great progress has been made in the last few years alone. Uncertainty in their distance scale has decreased by twenty orders of magnitude, and the error circle for angular position has shrunk by a factor of  $\sim$  billion. A large swath of progenitor theories have also been tentatively ruled out (Falcke & Rezzolla 2014; Kashiyama et al. 2013), leaving behind a minority of non-cataclysmic models. This came from work establishing their extraterrestrial (Petroff et al. 2015b) and later extragalactic (Masui et al. 2015) nature, as well as the discovery that FRB 121102 repeats (Spitler et al. 2016; Scholz et al. 2016). More recently, Chatterjee et al. (2017) were able to localize the repeating burst using the VLA, leading to the first unambiguous host galaxy identification. The host was found by Tendulkar et al. (2017) to be a low-metallicity, star-forming dwarf galaxy at  $z \approx 0.19$ . Marcote et al. (2017) used the European VLBI Network to study the radio counterpart, and favor either a low-luminosity AGN (discussed in Romero et al. 2016) or a young neutron star in a supernova remnant (proposed by Connor et al. (2016b); developed by Piro 2016; Murase et al. 2016; Lyutikov et al. 2016; Metzger et al. 2017) as the progenitor to FRB 121102. In the absence of multiple host-galaxy identifications, the  $\log N - \log S$  test is a useful method of indirectly determining the radial distribution of FRBs. The volume of the Universe is greater at larger distances, so there tend to be more faint events than bright ones. Because of this, the sensitive, single-dish telescopes that, to date, have discovered all FRBs, have detected mostly moderate-brightness events due to their limited FoV. Therefore, the high- $S$  tail of the FRB distribution has not yet been thoroughly explored. We parametrize the brightness distribution as a simple power-law, such that

$$dN \propto S^{-(\alpha+1)} dS, \quad (1)$$

where  $S$  is flux density and  $N$  is number of events. When integrated, this gives  $N(> S) \propto S^{-\alpha}$ , which we refer to as the brightness distribution. This one-parametric class of models has a single special value,  $\alpha = 3/2$ , corresponding to a non-evolving population of sources in a Euclidean spacetime. It is worth pointing out that this value is not limited to standard candles, so long as there is no statistical relationship between distance and luminosity or volume density. The  $3/2$  case also holds for anything proportional to flux density, so fluence or signal-to-noise can be used in place of  $S$ .

Several groups have tackled the  $\log N - \log S$  problem. Vedantham et al. (2016) argued that a surplus of multi-beam detections at Parkes implied a comparatively flat fluence distribution, with  $0.52 < \alpha < 1.0$ . Oppermann et al. (2016) used the ratio of observed signal-to-noise,  $s$ , to the search threshold,  $s_{\min}$ , to test the Euclidean hypothesis, motivated by the fact that it is model independent and does not suffer from survey incompleteness. This essentially reinstituted the classic  $\langle V/V_{\max} \rangle$ -test that was used to show the cosmological nature of quasars (Schmidt 1968) and gamma-ray bursts (GRBs; Mao & Paczynski 1992). They found consistency with a Euclidean distribution, but neither the Lorimer burst (Lorimer et al. 2007) nor FRB 150807 (Ravi et al. 2016, then-unpublished) were included in their analysis, whereas Vedantham et al. (2016) used both. Siemion et al. (2012) carried out a wide-field FRB search in “Fly-Eye” mode on the Allen Telescope Array (ATA) with roughly one quarter the exposure of our Pathfinder survey, though too few FRBs had been observed at the time to put limits on  $\log N - \log S$ . Vedantham et al. (2016) concluded separately that ATA’s non-detection rules out  $\alpha \lesssim 0.6$ . Macquart & Johnston (2015) argued that the apparent deficit of events at low Galactic latitudes may be explained by a steep brightness distribution, with  $\alpha > 2.5$ . However, such steep  $\log N - \log S$  are now disfavored by the data.

If Vedantham et al. (2016) are correct and the brightness distribution is much flatter than expected, then the implications for survey design are striking. They point out that for  $\alpha < 1$ , small dishes are actually preferred to large dishes because the high number of bright events favors sky coverage over sensitivity. Survey speed,  $\Gamma$ , which we take to be the rate at which a given experiment detects FRBs, is given by the product of field of view and a thermal sensitivity term raised to the power of  $\alpha$ . Sensitivity increases with collecting area, which scales quadratically with dish diameter,  $D$ , and beam-size goes as  $1/D^2$ . Therefore,

$$\begin{aligned} \Gamma &\propto \text{FoV} \times \text{sensitivity}^\alpha \\ &\propto D^{2(\alpha-1)}, \end{aligned} \quad (2)$$

and survey speed decreases with increasing dish size for flat distributions ( $\alpha < 1$ ). Using an incoherent-beam search on the pre-existing Canadian Hydrogen Intensity Mapping Experiment (CHIME) Pathfinder, we are able to test the low- $\alpha$  hypothesis with limited time on sky, based on similar arguments. The incoherent beam is generated by adding up the signals from all antennas after squaring their voltage time streams, erasing relative phase information. This produces a less sensitive beam

than the coherent case, for which phase is preserved, but is the size of the full primary beam.

We expect a coherent beam from  $N_a$  dual-polarization antennas will be  $\sqrt{N_a}$  times more sensitive than an incoherent beam from the same set of inputs, assuming noise is mostly uncorrelated between receivers. The factor of  $N_a$  in incoherent beam solid angle ultimately wins though—dramatically so for small  $\alpha$ , as can be seen by comparing the dark grey and orange regions in Fig. 1. If we take the ratio of the incoherent survey speed to coherent survey speed, assuming equal bandwidth and signal-to-noise cut-off, we get,

$$\begin{aligned} \frac{\Gamma_{\text{inc}}}{\Gamma_{\text{coh}}} &= \frac{N_a \Omega_i}{\Omega_i} \times \left( \frac{\sqrt{N_a} G_i / T_{\text{sys}}}{N_a G_i / T_{\text{sys}}} \right)^\alpha \\ &= N_a^{1-\alpha/2}, \end{aligned} \quad (3)$$

where  $G_i$  and  $\Omega_i$  are the gain and beam solid angle of a single feed. The Pathfinder, for which  $N_a = 128$ , should benefit from a factor of about 23 in speed-up for  $\alpha = 0.7$  when going from a coherent to an incoherent beam.

The “full” CHIME FRB project is expected to see multiple events per day, making it the fastest survey on sky (Connor et al. 2016a; Chawla et al. 2017). This is mainly due to its ability to search all  $\sim 10^3$  coherently-formed beams, with near 100% duty-cycle, filling its full  $\sim 200 \text{ deg}^2$  FoV primary beam at all times (Ng et al. 2017). Because full CHIME also has appreciable collecting area ( $8000 \text{ m}^2$ ), it is relatively  $\alpha$ -independent, which is also the case for fast upcoming surveys like APERTIF (van Leeuwen 2014) and UTMOST (Caleb et al. 2016). This is not true for the CHIME Pathfinder, which has a similar design to full CHIME, but less collecting area and its beam-forming backend is presently capable of processing only one synthesized full-polarization beam. This can be seen in Fig. 1, where we plot the expected number of detected FRBs per week as a function of  $\alpha$ , both for existing experiments and those in the commissioning stage. Large-FoV, highly-sensitive instruments like CHIME (light blue solid region) and APERTIF (dashed red curve; van Leeuwen 2014) are able to see faint events, as well as the rarer bright events. However, specialized instruments like the incoherent-beam CHIME Pathfinder (dark grey solid region) and the Deep Synoptic Array<sup>1</sup> (dashed black curve) are only competitive if  $\alpha$  is small. Moderate FoV instruments like the Parkes Multibeam Receiver and Arecibo’s ALFA are orders of magnitude faster than the incoher-

ent Pathfinder search for the Euclidean case, but several times slower if  $\alpha < 0.8$ .

In this paper we discuss the new incoherent-beam FRB survey on the CHIME Pathfinder. Its development was motivated by two points. Given its large instantaneous FoV but poor sensitivity, we could very quickly test the low- $\alpha$  hypothesis. And if  $\alpha$  really were significantly smaller than  $3/2$ , we would have set up—with little cost—a survey faster than the Parkes Multi Beam. We outline this experiment in Sect. 2, including the development of its beamforming and tree-dedispersion pipelines. In Sect. 3 we discuss our non-detection in  $\sim 53$  days of data and the constraints on  $\alpha$ . We then go over the implications for other similar surveys, and discuss various astrophysical reasons for our non-detection in Sect. 4.

## 2. CHIME PATHFINDER

A pathfinder instrument for CHIME was constructed at the Dominion Radio Astrophysical Observatory (DRAO) in Penticton, British Columbia, was brought online in late 2013 (Bandura 2014). Its purpose is to act as both a proof-of-concept instrument and a debugging tool for the full CHIME, whose highly ambitious primary science goal of 21 cm intensity mapping requires considerable precision in calibration. The Pathfinder consists of two north-south 37 m-long, 20 m-wide cylindrical mesh reflectors, whose focal lines are each instrumented with 64 linear dual-polarization antennas for a total of 256 inputs. This is roughly an order of magnitude smaller in scale than full CHIME, which has a total of 2048 inputs on four 100 m-long, 20 m-wide reflectors. More information about CHIME’s pathfinder instrument can be found in (Bandura 2014; Newburgh et al. 2014; Shaw et al. 2015; Berger et al. 2016).

The stationary, cylindrical reflector design makes CHIME a wide-field transit telescope. Since its dishes are aligned north-south, it only focuses light in the east-west direction, resulting in a primary beam that spans  $\sim 150^\circ$  in declination and  $1\text{--}2^\circ$  in hour-angle. North-south spatial resolution is recovered either by beamforming or computing the full  $N^2$ -correlation matrix, both of which are done in the Pathfinder’s correlator (for more details, see Recnik et al. 2015).

### 2.1. Beamformer

Since late 2015, we have had a working beamforming back-end in the Pathfinder. The beamformer is an OpenCL kernel run on a 16-node GPU cluster, which is the X-engine of the Pathfinder’s hybrid FX-correlator (Denman et al. 2015). It is run in a commensal mode with the more computationally intensive  $N^2$ -correlation

<sup>1</sup> [www.astro.caltech.edu/~srk/Workshop/BnE2016\\_NB.pdf](http://www.astro.caltech.edu/~srk/Workshop/BnE2016_NB.pdf)

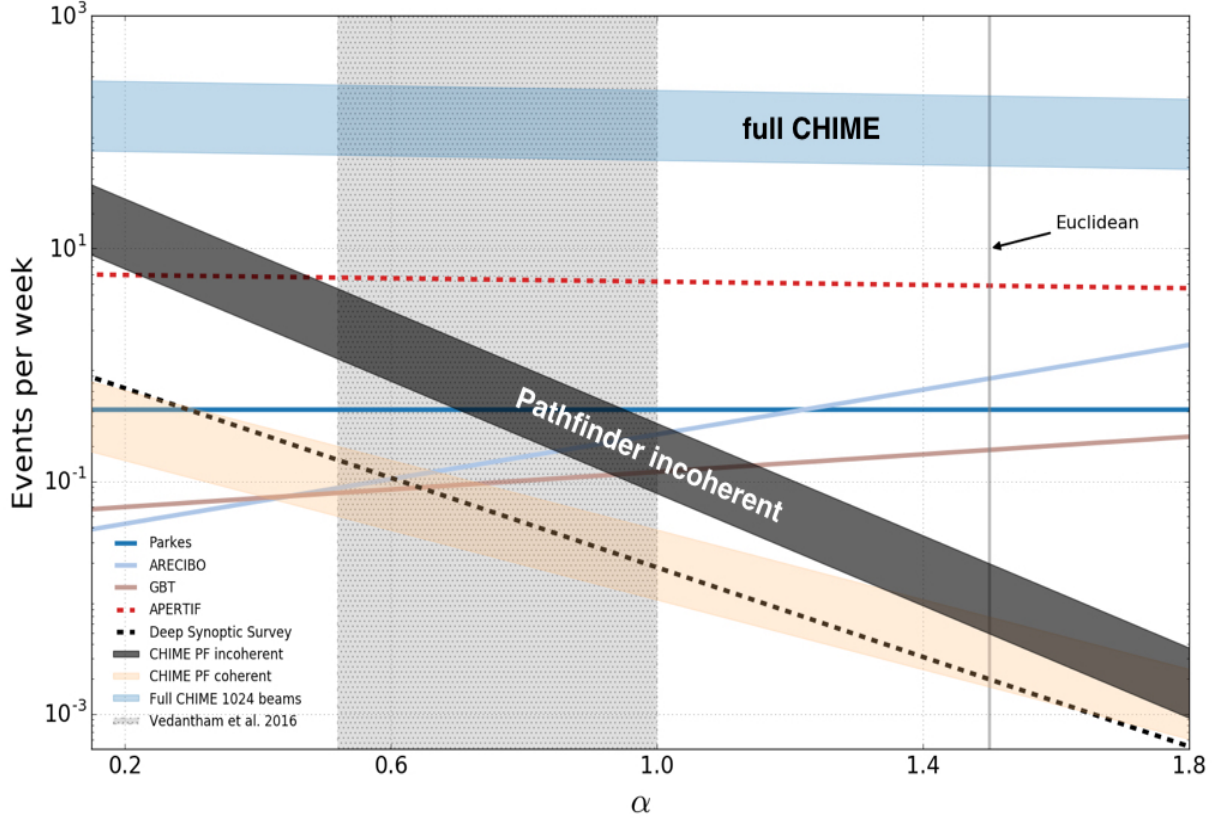


**Figure 1.** Weekly event rates for several different surveys plotted as a function of brightness distribution parameter  $\alpha$ , pinned to the Parkes rate (hence its flatness), similar to what is done in Eq. 11 with GBT. The three solid lines are surveys that have already found FRBs. The light grey dotted region shows the 90% confidence interval of  $\alpha$  proposed by Vedantham et al. (2016). The thick colored regions allow for uncertainty in the rate below 1.4 GHz, and the dashed curves are for 1.4 GHz surveys still in the commissioning phase. Interestingly, the modestly sized CHIME Pathfinder in incoherent mode (dark grey) would be the fastest survey to date in incoherent mode, if  $\alpha \lesssim 0.75$ . This is due to its 200 deg<sup>2</sup> primary beam and the importance of FoV for small  $\alpha$ .

that is used for the cosmology experiment. Initially, the beamformer produced a single coherent tracking beam that was used for pulsar observations and a preliminary FRB search. Once it was realized that an incoherent beam may potentially provide an enormous increase in search speed, the coherent beamforming kernel was modified to first square, then sum, incoming voltages. Channelized data arrive at each of the 16 GPU nodes from the custom F-engine electronics as 4-bit real, 4-bit imaginary offset encoded integers. Once these voltages are squared and summed across the array, they are reduced to 8-bit unsigned integers. Signals from all 256-inputs, but only one sixteenth of the frequencies, are processed on each node. The beamformed data are sent

to a separate acquisition node over a 10 Gigabit Ethernet at 6.4 Gbps in the VDIF specification<sup>2</sup>.

For the incoherent beamforming kernel, the intensities arrive at the acquisition node at full time and frequency resolution, 2.56  $\mu$ s and 390.625 kHz respectively. The squared and summed signals from our two orthogonal polarizations arrive separately, and are not summed until further down the pipeline. Since different frequencies arrive from different nodes, packets arrive out of order and must be unscrambled. A real-time, multi-threaded acquisition code was developed to handle this<sup>3</sup>. It writes to disk either assembled voltages (in the coherent beamforming case) or intensities integrated to 1.3 ms (in the

<sup>2</sup> [www.vlbi.org/vdif/docs/VDIF\\_specification.Release.1.1.1.pdf](http://www.vlbi.org/vdif/docs/VDIF_specification.Release.1.1.1.pdf)

<sup>3</sup> [https://github.com/kmsmith137/ch\\_vdif\\_assembler](https://github.com/kmsmith137/ch_vdif_assembler)



incoherent case). The latter are written to HDF5 files for offline processing. A diagram of the incoherent backend and search pipeline is shown in Fig. 2. The custom data processing pipeline was built specifically for this experiment.

## 2.2. FRB Search

We run a modified tree dedispersion algorithm on the data to search for FRBs with dispersion measures (DMs) between 20 and 2000  $\text{pc cm}^{-3}$  and widths between 1.3 and 100 ms. The package `burst_search`<sup>4</sup> was first developed to search GUPPI data from the Green Bank Telescope, and successfully found FRB 110523 (Masui et al. 2015). We modified this code to search both real-time Pathfinder data streams and offline, integrated intensity data. The data were broken up into 80-second total-intensity (Stokes I) arrays that overlapped by 15 s with the previous block. We do not search over spectral index. If the largest S/N value in a given block exceeded our threshold of 10, a trigger was written to disk, along with plots of the event. The large number of low-DM triggers jeopardized our seeing extragalactic events, so we searched ranges 20–200  $\text{pc cm}^{-3}$ , 200–525  $\text{pc cm}^{-3}$ , and 525–2000  $\text{pc cm}^{-3}$  separately.

### 2.2.1. RFI

Due to the incoherent beam’s sensitivity to the horizon, radio frequency interference (RFI) was a significant concern. When we searched raw data without any masking or de-trending, an event above the S/N threshold would occur in every processed block of data. A large fraction of these were due to the recently-introduced Long Term Evolution (LTE) wireless communication band around 700 MHz, which fluctuates on millisecond time-scales. By masking these and other persistent RFI frequency channels, most false positives could be avoided. But the data still needed preprocessing, so a series of filters was applied to each block of intensities before the tree-dedispersion search was run. This included a  $6\sigma$  outlier cut in frequency, which removes bad channels. Bandpass calibration is done by dividing our data by the time-averaged DC power within an 80-s block. We then apply a highpass filter that used a 100 ms Blackman window function, which sets our maximum search width. The effectiveness of this RFI-preprocessing was verified using transits from pulsar B0329+54, as well as simulations of FRB events; after preprocessing these events would be detected, but without the filtering, B0329+54 and injected events would go undetected due to strong RFI occurring during the

dispersed pulse. After pre-processing we reduced our false-positive rate to roughly one per 30 minutes.

## 2.3. Survey parameters

In order to estimate an expected FRB rate we need to know the telescope’s sensitivity, beamsize, and the effects of dispersion smearing, which can be difficult to determine. For example, the reduction in search speed of dispersion smearing is calculable only if the DM and width distributions of ultra-bright FRBs are known. Below we provide estimates of each of these quantities and their associated uncertainty.

### 2.3.1. Beamsize

Extensive work has been done both to simulate and map the primary beams of each Pathfinder antenna. Using the east-west holographic measurements made by Berger et al. (2016), and simulations of the north-south beam using the reflector antenna software GRASP<sup>5</sup>, we adopt half-power beam solid angles of 270, 225, 155, and 110 square degrees at 430, 525, 625, and 750 MHz, respectively. For most of our analysis we take their mean,  $\sim 190 \text{ deg}^2$ , to be our beamsize. However, it seems likely that this is a conservative estimate; early holography measurements indicate that the true north-south beam on-sky is larger than the beam produced in simulation.

### 2.3.2. Sensitivity

We were able to test our expected sensitivity using two distinct methods. The first method uses the fractional power increase from the transits of bright point-sources such as Cassiopeia A, Cygnus A, and Taurus A (Crab nebula), to estimate the baseline  $T_{\text{sys}}$ . This “Y-factor method” measures the average system temperature of the individual antennas, but does not measure the effective  $T_{\text{sys}}$  of our incoherent beam. The point-source transits give what we expect, namely an average system temperature per antenna of  $\sim 60 \text{ K}$  assuming an aperture efficiency of 50% (Davis 2012). The second method, which is more relevant to our search, comes from using the radiometer equation with measurements of single pulses of B0329+54, and indicates higher-than-expected noise. The difference between the two methods is that the latter measures an actual RMS of the final incoherent beam, so it probes the way the noise averages down after we sum across the array.

B0329+54 is the brightest visible pulsar in our band, and fortuitously is only  $\sim 5$  degrees off-zenith at our latitude. According to the Australia Telescope National Facility (ATNF) Pulsar Database, B0329+54 has flux

<sup>4</sup> [https://github.com/kiyo-masui/burst\\_search](https://github.com/kiyo-masui/burst_search)

<sup>5</sup> <http://www.ticra.com/products/software/grasp>

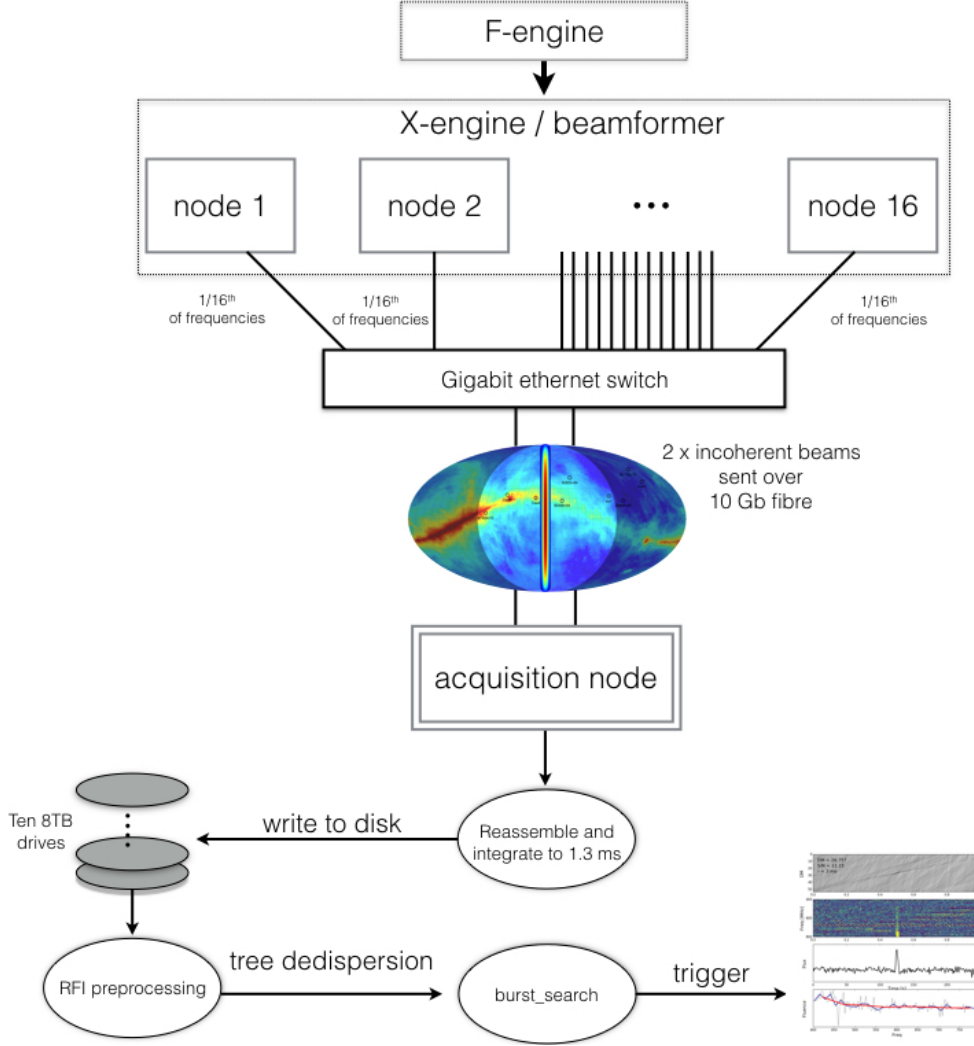


**Figure 2.** Block diagram outlining the Pathfinder’s incoherent-beam FRB search. Data are channelized in a 16-FPGA F-engine, sent to the beamforming kernel in a GPU-based X-engine, then sent to an acquisition node and written to disk. These intensities are searched offline using a tree-dedispersion code, after RFI preprocessing.

densities at 400 MHz and 1.4 GHz of  $S_{400}^\nu = 1500$  mJy and  $S_{1400}^\nu = 200$  mJy, respectively (Manchester et al. 2005). With a pulse width of 6.6 ms and a 714 ms period, its interpolated flux density at 600 MHz when it is “on” is 84 Jy, assuming a power-law index  $\gamma = 1.61$ . To calculate the expected S/N from a dedispersed, frequency-averaged time-series, the average flux,  $\langle S \rangle_\nu$ , can be estimated by summing in quadrature. This gives an effective flux density of  $\sim 96$  Jy. If we then measure the average S/N of single B0329+54 pulses, we can use  $\langle S \rangle_\nu$  to constrain the system’s sensitivity. This is done with the radiometer equation,

$$S/N = \frac{\langle S \rangle_\nu \sqrt{2B_{\text{eff}}\tau}}{S_{\text{sys}}}, \quad (4)$$

where  $B_{\text{eff}}$  is the effective bandwidth,  $\tau$  is the pulse duration, and the factor of 2 is the number of polarizations.  $S_{\text{sys}}$  is the system-equivalent flux density (SEFD), which is simply the ratio of system temperature to forward gain,  $T_{\text{sys}}/G$ . We opt for the SEFD since  $T_{\text{sys}}$  and  $G$  are often degenerate, and we do not need to distinguish between the two for our purposes.

From the several dozen B0329+54 transits we have in our dataset, over 50,000 individual pulses were observed. Analyzing the stored data, we find at beam center, the mean S/N was  $\sim 10$ , so  $S_{\text{sys}} = 2 \times 10^4$  Jy, using  $B_{\text{eff}}$  and  $\tau$  from Table 1. This is a few times larger than expected, which seems to be caused by excess noise on time-scales  $\lesssim 20$  ms, leading to larger RMS on all time-scales. This excess is also seen in the noise power spectrum at high

**Table 1.** Parameters of the CHIME Pathfinder and its incoherent FRB survey.  $N_a$  is the number of dual-polarization antennas, which is half the number of beamformer inputs.

	PARAMETER	VALUE
	$N_a$	128
<b>CHIME Pathfinder</b>	$A_{\text{geo}}$ [m <sup>2</sup> ]	880
	freq [MHz]	400–800
	$N_{\text{chan}}$	1024
	$S_{\text{sys}}$ [Jy]	$2 \times 10^4$
<b>Incoherent FRB search</b>	$T_{\text{obs}}$ [hrs]	1268
	$\Omega$ [deg <sup>2</sup> ]	190
	$B_{\text{eff}}$ [MHz]	312
	$s_{\text{min}}$ [ $\sigma$ ]	10
	$S_{\text{min}}^{\text{ms}}$ [Jy]	125
	Exposure [deg <sup>2</sup> hrs]	241,000

temporal frequencies, and may be caused by intermittent RFI. The discrepancy between the Y-factor method and the S/N of B0329+54 pulses would then come from correlated RFI-induced noise not beating down as  $\sqrt{N_a}$  as we sum all antennas in the beamformer.

We also collected roughly  $10^3$  Crab giant pulses (GPs). Due to their steep brightness distribution and uncertainty in absolute flux density, they were not directly used as a calibrator. However, by comparing to a large set of GPs observed in our band with the Algonquin Radio Telescope (Main et al., in prep), we find our rate of 2–8 GPs per minute with  $s > 10\sigma$  to be consistent with the brightness distribution they found.

### 2.3.3. DM Smearing

Though full CHIME will “upchannelize” its data (increase the frequency resolution after the initial channelization step) (Ng et al. 2017), the incoherent Pathfinder search was carried out with the nominal 1024 channels at 390-kHz resolution. This leads to “DM smearing” for highly dispersed events, which broadens the pulse and reduces S/N. If the FRB’s intrinsic width is  $t_i$ , is scattered to a width  $\tau$ , and is sampled at  $t_{\text{samp}}$ , the minimum flux density to which we are sensitive is increased as,

$$S'_{\text{min}} \rightarrow S_{\text{min}} \times \left( \frac{t_I}{\sqrt{t_{\text{samp}}^2 + \tau^2 + t_i^2}} \right)^{1/2}, \quad (5)$$

where  $t_I$  is the final pulse width (Burke-Spolaor & Banister 2014). Using  $\Delta\nu$  as the frequency resolution, and  $\nu_c$  as the central frequency, the effective pulse width can be calculated by adding in quadrature the other broadening elements. This is done as follows,

$$t_I^2 = \tau^2 + t_i^2 + t_{\text{samp}}^2 + t_{\text{DM}}^2 \quad (6)$$

where

$$t_{\text{DM}} = 8.3 \left( \frac{\text{DM}}{\text{pc cm}^3} \right) \left( \frac{\Delta\nu}{1 \text{ MHz}} \right) \left( \frac{\nu_c}{1 \text{ GHz}} \right) \mu\text{s}. \quad (7)$$

In this survey the smearing term will dominate the sampling time and, probably, intrinsic width, for high DMs. Scattering is less constrained. For example, a burst with DM=776 pc cm<sup>−3</sup> (the median DM on FRBcat Petroff et al. 2016) that was intrinsically 1 ms, sampled at 1.3 ms, and scattered to 5 ms (roughly the case for GBT FRB 110523 if it were observed at 600 MHz), would be  $\sim 12$  ms in duration if observed on the Pathfinder. Therefore, if all FRBs had the parameters of that hypothetical burst, Eq. 5 tells us that the current Pathfinder search would be  $\sim 6^{\alpha/2}$  times slower than a sufficiently upchannelized Pathfinder search. But not all FRBs will have those exact parameters, and the number of degrees of freedom in Eq. 6 makes predicting the effects of smearing for high-DM events difficult.

Fortunately, there is reason to think this would not be a major issue. The only way the incoherent-beam Pathfinder search will see anything is if  $\alpha$  really is small (see the low detection rate for  $\alpha > 1.2$  in Fig. 1). That would mean the IGM is doing a significant fraction of the dispersion, in which case brightness anti-correlates with DM, as nearby sources have less intervening plasma. In other words, our survey only probes the ultra-bright, nearby subset of the FRB population, and their low DMs will not greatly reduce the survey’s sensitivity. Indeed, the two sources whose inferred flux density was orders-of-magnitude greater than the FRB median (the Lorimer burst and FRB 150807) both had extragalactic DMs less than 350 pc cm<sup>−3</sup> (Lorimer et al. 2007; Ravi et al. 2016).

## 3. RESULTS

In 1268 hours of data several thousand triggers were produced with signal-to-noise greater than 10. Each was inspected by eye, and almost every “event” was discernibly non-astronomical. For example, the incoherent beam’s susceptibility to RFI means that most triggers were narrow-band or had unusual discontinuities in their frequency-collapsed profile. As discussed in Sect. 2.2.1,



some of these false-positives were caused by strong interference flickering on time-scales of tens of milliseconds. The handful of marginal events were analyzed further, but no FRBs were found. Having seen zero events, we can ask how unlikely that outcome was and therefore put a lower limit on  $\alpha$ . But first, we must verify that if there were an FRB in our beam, we would have detected it.

### 3.1. Completeness

There are many ways for a transient search to not see something, so care must be taken in verifying a survey’s completeness and reliability. Since the incoherent beam-former does not do any spatial filtering, we see the whole northern sky each day with CHIME’s large north-south primary beam. Giant pulses (GPs) from the Crab and single pulses from B0329+54 were used to ensure the search pipeline was working and that each day’s data were good. All other pulsars—including GP-emitting sources like B1937+21—are too faint to see individual pulses. This is also true for known RRATs. For the two sources we could see, we found that, even when the sources were entering the beam and the maximum S/N in a given 80-s block was around our search’s threshold,  $s_{\min}$ , individual pulses still triggered and were easily recognizable as pulses. We detected B0329+54 pulses and Crab GPs in all of their respective transits during our observing campaign. However, getting a fractional completeness—the ratio of the number of detections to number of events—is difficult for these sources. This is due to their pulse-to-pulse intensity fluctuations, which cause their S/N to fall below our threshold, and the fact that we trigger only on the brightest event above  $10\sigma$  in each 80-s block of data. In order to quantify our fractional completeness, we injected signals into our data with  $\text{DM} = 400 \text{ pc cm}^{-3}$  at a range of brightnesses. We find that for the injected signals whose expected resultant  $\text{S/N} \gtrsim 15$ , effectively all pulses are recovered and our completeness is above 99%. For events whose recovered S/N is between 10–12, we detect  $\sim 90\%$  of the simulated bursts. Fortunately, as we show in Fig. 4, for  $N(> S)$  power-laws with  $\alpha < 1.5$ , most FRBs are expected to be detected above  $15\sigma$ .

Two examples of the output of our search are seen in Fig. 3, which show four different visualizations of the data for each event. The top panel of each trigger plot shows the burst’s amplitude in DM / arrival time space. The second panel from the top shows a frequency / time intensity array after dedispersing the pulse to the maximum likelihood DM. The next panel shows a frequency-averaged pulse profile, and the final panel shows fluence plotted against frequency for three different binnings.

The B0329+54 trigger illustrates that pulses near the cut-off are still easily identifiable. The Crab trigger shows that high-S/N events are not excised by our RFI-preprocessing.

The clarity of B0329+54 pulses or Crab GPs close to  $10\sigma$  is in stark contrast to the vast majority of unexpected triggers. Several thousand events were inspected by eye, almost all of which were unequivocally false positives. They would have power only in a few frequency channels, or would look like step-functions in time. The borderline events were followed up by analyzing directly the data around the event, but ultimately there were no triggers that looked like broad-band, single-DM pulses. The triggers produced tended to be very low DM, which is why we partitioned the full DM range into three groups. RFI triggers cluster around the minimum search DM as well as the signal-to-noise threshold. The latter effect is shown in Fig. 4. The light purple histogram is the S/N distribution of 3470 triggers. Almost half of them had  $10 \leq s \leq 11$ , whereas only 7% and 13% of FRBs would be within  $1\sigma$  of the threshold, assuming  $\alpha = 0.75$  and  $\alpha = 1.5$  respectively.

### 3.2. Constraints on $\alpha$

If we treat the arrival times of detectable FRBs as Poissonian, we can calculate the probability of seeing  $M$  events given some expected number of events  $\mu$ . The expected number of events will depend on  $\alpha$ , so this likelihood can be written as,

$$P(M|\alpha, \mu) = \frac{\mu^M(\alpha) e^{-\mu(\alpha)}}{M!}. \quad (8)$$

A suitable model for  $\mu$  must now be chosen. Assuming a homogeneous Poisson process, the expected number of events in a given interval is proportional to the duration of that interval and the area of sky covered. This can be written as

$$\mu = r_0 \Omega T_{\text{obs}} \quad (9)$$

where  $T_{\text{obs}}$  is the total searchable observing time and  $r_0$  is the true rate on the sky per unit time and solid angle. We follow Connor et al. (2016a) and tether our expected rate to the empirical rate of a similar survey with detections. This is more direct than the standard method of rate estimation which quotes an all-sky rate above some fixed fluence threshold and then scales accordingly with  $\alpha$ . This also eschews the need to choose a single fluence completeness value, or make assumptions about the distribution of pulse widths, and relaxes the need to account for non-uniform sensitivity over the FoV. The Green Bank Telescope Intensity Mapping (GBT IM) survey is a natural reference point, since

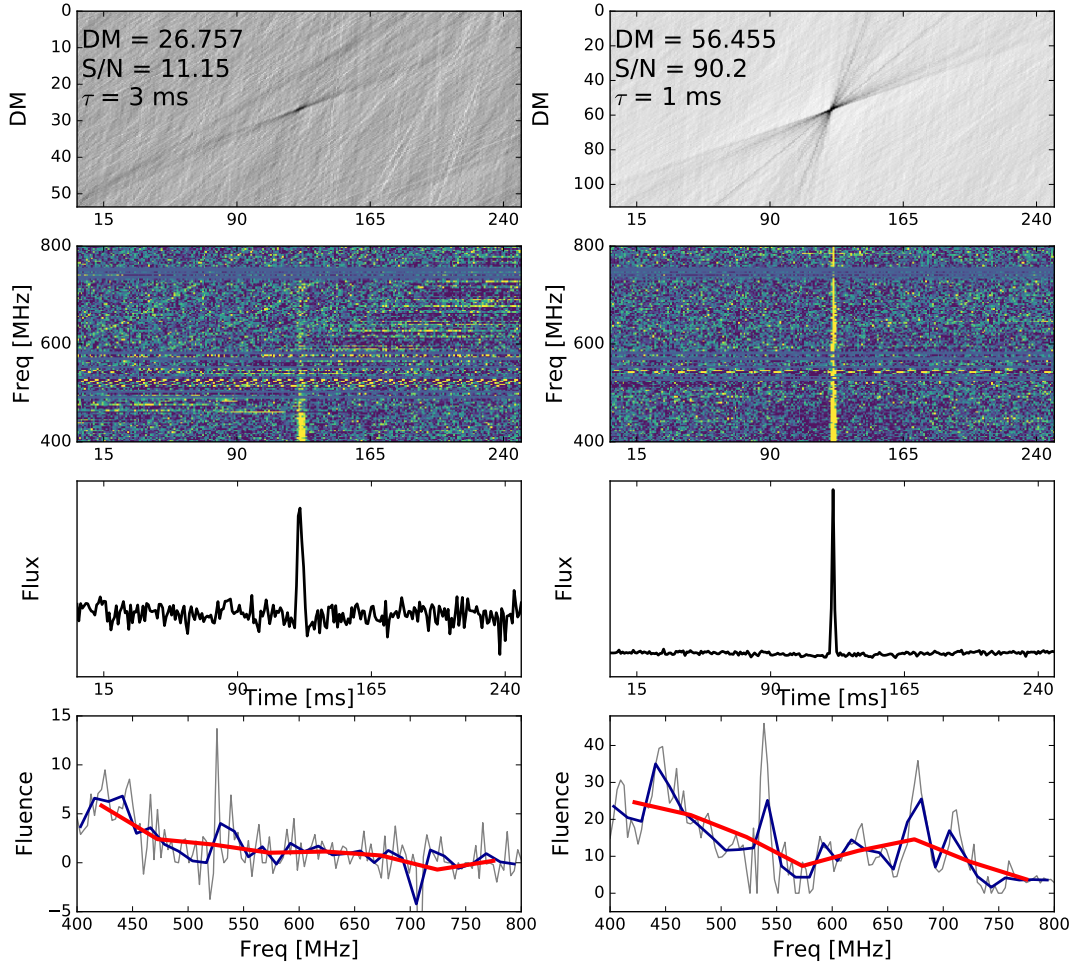


**Figure 3.** Example triggers from our `burst_search` pipeline. Each “event” produces a figure with four panels. From top to bottom: amplitude in DM vs. arrival time; the dedispersed intensity in frequency and time; the frequency-collapsed pulse profile; and a fluence spectrum of the pulse for three different binnings. The left figure shows a typical single pulse from B0329+54 with  $s \sim 11$ . Even when events were right around  $s_{\min}$ , Crab GPs and B0329+54 pulses were unambiguously celestial, in the sense that they were broad-band, isolated in DM vs. arrival time, and were detected as single peaks in the frequency-collapsed pulse profile. This is promising given none of the unexpected triggers had this property. The right figure shows a high-significance Crab GP, with  $s \sim 90$ . This established that our RFI-preprocessing should not remove ultra-bright events, even in the presence of significant frequency structure.

it found the only published FRB below 1.4 GHz and it overlaps with the CHIME band at 700–800 MHz. While the GBT rate is consistent with the rate at 1.4 GHz, it is more uncertain. To account for this, we can marginalize over the low-frequency event-rate uncertainty from GBT. One could also use the more precisely determined rate from Parkes (Champion et al. 2016), but then un-

certainities about scattering and spectral index are introduced. We discuss this point further in Sect. 4.

We can now write down a relationship between the rate inferred from GBT with the number of events we

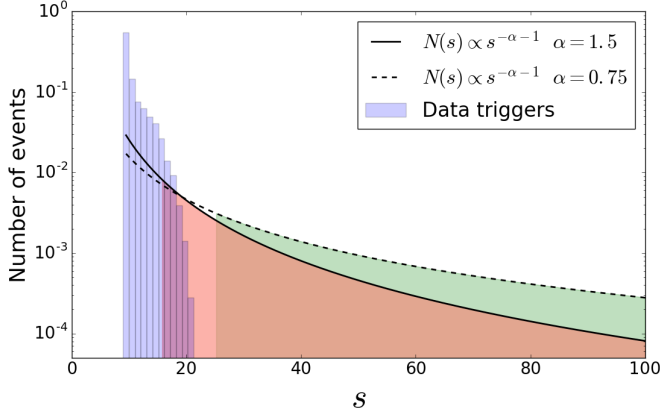


**Figure 4.** A comparison between the S/N distribution of false positive triggers found in the data with the distribution expected for FRBs. The purple histogram shows the normalized S/N counts for 3470 triggers in the data, each inspected by eye. The solid and dashed curves show the expected power-laws with  $\alpha = 1.5$  (Euclidean) and  $\alpha = 0.75$ , respectively. The shaded region under each curve represents half of the probability mass, meaning for the values of  $\alpha$  that this survey can probe, 50% of events should have higher S/N than any false-positive in the dataset.

expect to see at the Pathfinder. The GBT rate is scaled in the following way

$$\mu_{\text{PF}} = \mu_{\text{GBT}} \frac{N_{\text{days}}^{\text{PF}}}{N_{\text{days}}^{\text{GBT}}} \times \frac{\Omega_{\text{PF}}}{\Omega_{\text{GBT}}} \times \left( \frac{H_{\text{GBT}}}{H_{\text{PF}}} \right)^{\alpha}, \quad (10)$$

where  $H$  is a thermal sensitivity term given by the survey’s bandwidth,  $B$ , its SEFD,  $S$ , and its signal-to-noise cut-off,  $s_{\text{min}}$ . Given that GBT saw one event in 27.5 days with a beamsize of  $0.055 \text{ deg}^2$ , 200 MHz of bandwidth, and a signal-to-noise threshold of 8, we can write this relationship more explicitly. We expect the following number of events,

$$\mu_{\text{PF}} = \mu_{\text{GBT}} \frac{N_{\text{days}}^{\text{PF}}}{27.5} \times \frac{\Omega}{0.055 \text{ deg}^2} \left( \frac{13.25 \text{ Jy}}{S_{\text{sys}}} \right)^{\alpha} \left( \frac{B}{200.0 \text{ MHz}} \right)^{\alpha/2} \times \left( \frac{\sqrt{\tau^2 + t_i^2}}{t_I} \right)^{\alpha/2} \left( \frac{8}{s_{\text{min}}} \right)^{\alpha}. \quad (11)$$

In Eq. 11  $\mu_{\text{PF}}$  is the expected number of events for the incoherent Pathfinder, and  $\mu_{\text{GBT}}$  is the expected number of events in 27.5 days of observing with GBT. The latter has a maximum-likelihood value of 1 and a 95% confidence interval of 0.25–5.57 (Connor et al. 2016a).

We assume GBT’s SEFD to be  $26.5 \text{ K} / 2.0 \text{ K Jy}^{-1}$ , and we have included a DM smearing term, which we take to be negligible in the case of Green Bank. We use  $\text{DM} = 500 \text{ pc cm}^{-3}$ , based on the argument in Sect. 2.3.3 that we are only sensitive to nearby, and therefore relatively low-DM FRBs. One advantage of directly extrapolating from the empirical rate of another survey is that we do not need to compute an integral under the beam to account for direction-dependent sensitivity; the correction factors from the two surveys roughly divide out. However, the effect must be accounted for when quoting “all-sky” rates, especially if the telescope has significant sidelobes.

Using the values in Table 1, we can calculate the expected number of events,  $\mu$ , for each value of  $\alpha$  and compute the probability of non-detection with the likelihood function in Eq. 8. If we were to ignore uncertainty in the rate, we would simply apply a  $p$ -test using the maximum-likelihood value in Eq. 11, and ask what values of  $\alpha$  can be ruled out with, say, 95% certainty. But in general,  $r_0$  and  $\alpha$  are degenerate (Oppermann et al. 2016). In the case of our non-detection, we cannot strictly differentiate between small- $\alpha$  with a low rate, and large- $\alpha$  with a high rate. Therefore, we marginalize over the uncertainties in the true sky rate, similar to what is done by Oppermann et al. (2016). Mathematically, this is just the sum of likelihood curves for all rates,  $r_0 > 0$ , weighted by the probability density at that rate,  $\mathcal{P}(r_0)$ . We use the GBT rate posterior as  $\mathcal{P}(r_0)$ , and compute the following integral,

$$P(M=0|\alpha) = \int_0^\infty P(0|\alpha, r_0) \mathcal{P}(r_0) dr_0. \quad (12)$$

This procedure produces the black curve shown in Fig. 5. The curve is equal to 0.05 at  $\alpha \approx 0.9$ , meaning if  $\alpha$  were smaller than 0.9, we would have expected to see one or more FRBs in 53 days of Pathfinder data > 95% of the time. The figure also shows the non-detection likelihoods for a range of event rates. The green region shows the likelihood values for rates between 0.34–4.68 times the maximum-likelihood rate. 0.34 is the value above which 95% of the GBT rate posterior lies, and 4.68 is the upper-bound on 95% of the posterior.

## 4. DISCUSSION

### 4.1. Brightness-dependent $\alpha$

The most model-independent statement we can make about our results is not about  $\alpha$ , but about the event rate above our sensitivity threshold, between 400–800 MHz. Turning that rate upper-limit into a lower-limit on  $\alpha$  requires some assumption about the functional form of the brightness distribution, and its scaling

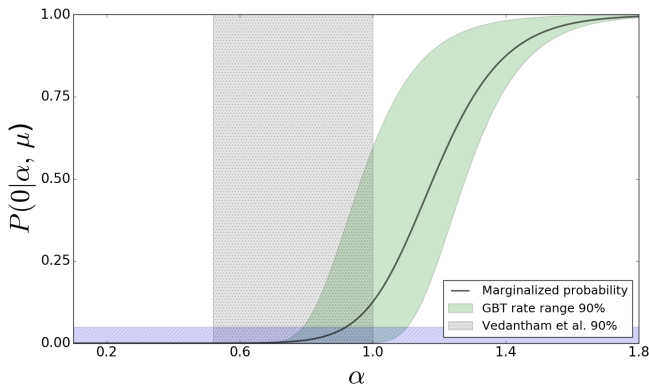


**Figure 5.** Probability of detecting zero events in 53 days of incoherent Pathfinder data, plotted as a function of the brightness distribution parameter  $\alpha$ . The black curve shows the probability of seeing no FRBs, marginalized over uncertainty in the GBT rate. The green shaded region is bounded by the 95% lower-limit on the GBT rate (left) and the 95% upper-limit (right). The light blue hatched region shows where the probability is less than 0.05, implying that we can rule out with 95% confidence  $\alpha < 0.9$ .

(i.e. the true rate on the sky). For example, we have assumed the distribution’s shape is described by a single power-law. But for a large enough range of brightnesses and an underlying cosmological population, the one-parameter power-law assumption breaks down (see the light blue curve in Fig. 6). Ignoring, for a moment, the Universe’s star-formation history and considering only non-Euclidean effects, we generically expect a relative deficit of faint events. This is because FRBs at large distances will be diminished in energy and rate due to cosmological redshift and time dilation. Therefore,  $\alpha$  is brightness-dependent, flattening out for high- $z$  sources and asymptoting to  $3/2$  as  $z_{\text{src}}$  approaches 0, with a simple mapping between brightness and redshift in the idealized standard-candle case. This phenomenon is seen in  $\log N$ – $\log S$  of long GRBs, which exhibit such a continuously varying  $\alpha$  parameter, and is nearly flat at the fluences of the faintest bursts. In the bright tail, the curve approaches a power-law with index  $3/2$  (Nava et al. 2011, Fig.1). One consequence of this is that surveys with different sensitivities will measure different  $\log N$ – $\log S$  slopes. For example, the distribution of FRB signal-to-noise within a low-sensitivity survey may be Euclidean, even though a flatter distribution might be required when extrapolating to the rates of larger telescopes. Oppermann et al. (2016) provide a framework for constraining  $\alpha$  based on S/N distributions as well as detection counts between surveys.

We justified our constant- $\alpha$  assumption for the CHIME Pathfinder by pointing out that we were probing flux densities that are only a couple of orders-of-magnitude larger than where most FRBs have been seen ( $\sim$ ten times closer, on average), and so the effects of brightness-dependent  $\alpha$  might be negligible. However, it is possible that  $N(> S)$  turns over at a flux density that is less than our threshold, and approaches  $\alpha \approx 1.5$  the way the brightest GRBs do.

#### 4.2. Consistency with the ultra-bright rate

The brightest event at the time of this publication, FRB 150807, would probably not have been detectable in our survey, in part because it was narrower than our sampling time and its S/N would be reduced (Ravi et al. 2016). Despite not having seen anything, we can ask if the rate of ultra-bright events implied by 150807 and the Lorimer burst is in agreement with our results, for a given value of  $\alpha$ . Ravi et al. (2016) predict that the rate at 1.3 GHz of FRBs above 50 Jy ms is  $190 \pm 60 \text{ sky}^{-1} \text{ day}^{-1}$ . Using  $\alpha = 3/2$  and a minimum burst energy of 220 Jy ms with width 5 ms, the quoted rate predicts one every couple of months in our current configuration. In other words, our non-detection could be consistent with  $190 \pm 60 \text{ sky}^{-1} \text{ day}^{-1}$  if those ultra-bright events are, on average, from nearby sources, and the required extrapolation is near-Euclidean. On the other hand, an  $\alpha = 0.7$  extrapolation predicts roughly one per week, which is not consistent with our data. Of course, our non-detection is also consistent with the rate of Ravi et al. (2016) having been overestimated.

#### 4.3. 600 MHz vs. 1.4 GHz

Our results are the first constraints at 600 MHz, but several surveys have searched, to no avail, at lower frequencies (Tingay et al. 2015; Coenen et al. 2014). Karastergiou et al. (2015) searched around 140 MHz with LOFAR and saw nothing, though inter-channel smearing meant they had a maximum DM of just  $320 \text{ pc cm}^{-3}$ . A GBT survey at 350 MHz placed a 95% confidence upper-limit of a few thousand detectable FRBs per sky per day after searching  $\sim 80$  days of data (Chawla et al. 2017). This result is still roughly consistent with the rate at 1.4 GHz, which has a lower bound around  $10^3 \text{ sky}^{-1} \text{ day}^{-1}$  (Oppermann et al. 2016; Champion et al. 2016). Nevertheless, the uncertainty in FRB rate as a function of frequency is a concern for us. We have tried to mitigate its effects by tying the Pathfinder results to the only published FRB survey in our band, and marginalizing over the rate distribution. Still, the GBT IM survey only overlaps with ours at the top of the CHIME band, between 700–800 MHz. If the



effects of scattering, free-free absorption, and smearing are significantly more destructive in the bottom of our band, then we would have overestimated the effective rate and, consequently, our lower-limit on  $\alpha$ .

In spite of the spectral uncertainty in rate, the brightness distribution’s logarithmic slope,  $\alpha$ , should be fairly robust against frequency variation. The spectral behaviour of FRBs does affect the shape of  $N(> S)$  in the cosmological case, but at a given value of  $S$ , there are only special cases where  $\alpha$  is frequency-dependent. If the intrinsic source luminosity is given by a power-law,  $\mathcal{L} \propto \nu^\gamma$ , then we will observe the part of the spectrum that has been redshifted down to our instrument’s band. Negative spectral index lowers the observed energies of distant FRBs as,  $\mathcal{L} \rightarrow \mathcal{L}(1+z)^\gamma$ , thereby decreasing the number of visible distant events and flattening  $\log N - \log S$ . Conversely, positive  $\gamma$  steepens it. These effects are shown in a toy-model plotted in Fig. 6. While the curves all approach the Euclidean value of  $3/2$ , there is significant spectral index dependence in  $\alpha$  for FRBs when cosmological volumes are probed. If the source has non-power-law frequency behaviour (e.g.  $\sim$  GHz scintillation), then the source-to-source (or even pulse-to-pulse) variance in brightness will increase, but the ensemble distribution should not be affected unless there is an average tilt in FRB spectra.

#### 4.4. Implications for other surveys

The CHIME Pathfinder’s incoherent-beam survey is searching a limited region of FRB parameter space, namely the ultra-bright tail between 400–800 MHz. Because of this large brightness threshold, our results have few implications for full CHIME, which will have a flux density limit that is several hundred times lower than the current search, thanks to its coherent beams and larger collecting area. Therefore, the primary uncertainty in full CHIME’s rate of detection—the deleterious effects of scattering and/or free-free absorption at low frequencies—remains. But as Connor et al. (2016a) showed, even if the rate between 400–700 MHz is zero, CHIME’s overlap with GBT IM between 700–800 MHz indicates that it will see multiple bursts per day, assuming current design parameters. Chawla et al. (2017) also found a large event rate, accounting for scattering and spectral index. Upcoming surveys like UTMOST (Caleb et al. 2016) and APERTIF (van Leeuwen 2014) will also unite sensitivity with FoV. Therefore, their speed is largely  $\alpha$ -independent, unless they are not operating at full capacity, e.g. during commissioning. Detections made in the commissioning phase, before design sensitivity is reached, could address our claims about

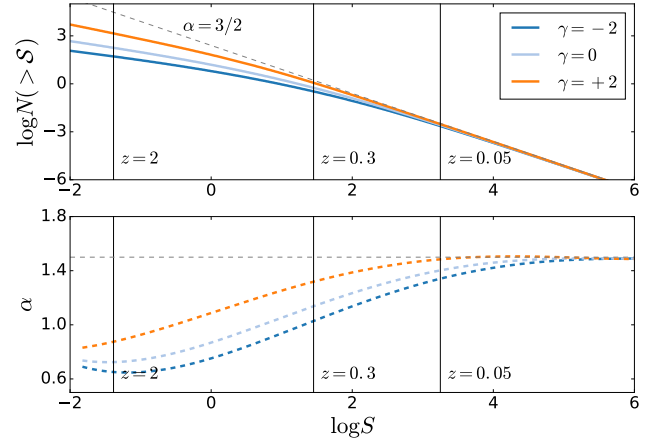


**Figure 6.** Simulated flux density distribution assuming standard candles with varying spectral index,  $\gamma$ , meant to highlight how non-Euclidean effects and spectral index alter  $\alpha$ . The top panel shows  $N(> S)$  as a function of  $S$ . The bottom panel shows  $\alpha$ , which is the slope of these curves in logspace. In the standard candle scenario, there is a one-to-one mapping from fluence to redshift for a given spectral index. The vertical lines show that mapping for the  $\gamma = 0$  case to give an idea of the size of cosmological effects at each redshift. In the non-standard candle case, these effects are still seen so long as the statistics of intrinsic luminosity function do not evolve with distance.

brightness-dependent  $\alpha$ , since those early, bright bursts, may have a Euclidean distribution.

The non-detection does, however, have implications for other lower-sensitivity surveys. The Deep Synoptic Array (DSA) initially will consist of ten 5-m dishes combined incoherently, in the hopes of detecting ultra-bright FRBs. Saving to disk buffered voltage data could achieve  $\sim$  arcsecond localization, allowing for a very high-impact survey on a moderate budget. However, if  $\alpha$  is not significantly smaller than 1.5, then that survey may not detect an event for many months. Extrapolating from the Parkes Multi Beam rate of one event every couple of weeks, we estimate that the DSA would have to wait of order a year per FRB if  $\alpha \approx 1.1$ . However, given the importance of localization, a scaled-up DSA with more dishes could prove highly valuable. In a similar vein, the Australian Square Kilometre Array Pathfinder’s (ASKAP) small dishes and phased-array feeds will effect large sky coverage with long baselines, potentially providing regular localization (Macquart et al. 2010).

## 5. CONCLUSIONS



We have performed a shallow, wide-field FRB survey using the CHIME Pathfinder. This was motivated by recent assertions about the flatness of the brightness distribution of FRBs by [Vedantham et al. \(2016\)](#), who showed that  $\alpha$  may be less than 1. If this were the case, the incoherent-beam Pathfinder search would be a highly competitive survey, potentially detecting multiple events per week. And if  $\alpha$  were not quite so low, our search could demonstrate this with relatively little time on sky. We took 52.85 days of data, amassing an enormous exposure, with  $\sim 2.4 \times 10^5 \text{ deg}^2 \text{ hrs}$ . These data were searched using tree-dedispersion software that was used to discover FRB 110523 ([Masui et al. 2015](#)). Thousands of triggers above our S/N threshold of 10 were produced, including daily Crab GPs and B0329+54 pulses, but no FRBs were found. By not detecting anything FRB signatures we are able to rule out  $\alpha < 0.9$  with 95% confidence, using the GBT 700–900 MHz rate and assuming the single-index power-law approximation holds into our flux sensitivity. This constrains the number of events brighter than  $\sim 220\sqrt{(\tau/\text{ms})} \text{ Jy ms}$  for  $\tau$  between 1.3 and 100 ms to fewer than  $\sim 13 \text{ sky}^{-1} \text{ day}^{-1}$ . We quote our upper-limit in this way because surveys have a single signal-to-noise threshold, but in fluence space this cut-off is a curve that depends on pulse width. The sub-arcsecond localization of FRB 121102 has shown that FRBs are distant enough that non-Euclidean effects ought to be significant. Still, its considerable local dispersion means that the IGM contribution is only about half of 121102’s extragalactic DM ([Tendulkar et al. 2017](#)). If local dispersion were a generic property of FRBs, then the volumes that modern sur-

veys are sensitive to would shrink and deviation from  $\alpha = 3/2$  should be decreased, other things being held equal.

As the lower-limit on  $\alpha$  increases, the incoherent-beam Pathfinder search experiences diminishing returns in its ability to constrain. For example, with just 5 days on sky,  $\alpha \lesssim 0.6$  can be ruled out by a non-detection with 95% confidence. As we have shown,  $\sim 53$  days sets a lower-bound of 0.9, but zero events in an entire year on sky can only rule out  $\alpha \lesssim 1.15$ . For this reason, if we choose to run the incoherent-beam Pathfinder search indefinitely, the best strategy is to increase its sensitivity. This would mean investigating further the larger-than-expected noise fluctuations on short time-scales, perhaps mitigating it with baseband RFI removal. The null result suggests similar wide-field low-sensitivity surveys may not be highly competitive, but has little implication for wide-field deep surveys like full CHIME, APERTIF, and UTMOST.

We are very grateful for the warm reception and skillful help we have received from the staff of the Dominion Radio Astrophysical Observatory, which is operated by the National Research Council of Canada. The CHIME Pathfinder is funded by grants from the Natural Sciences and Engineering Research Council (NSERC), and by the Canada Foundation for Innovation (CFI). LC acknowledges that the research leading to these results has received funding from the European Research Council under the European Union’s Seventh Framework Programme (FP/2007-2013) / ERC Grant Agreement n. 617199. We also thank Manisha Caleb and Casey Law for useful discussions.

## REFERENCES

- Bandura, K. e. a. 2014, in Society of Photo-Optical Instrumentation Engineers (SPIE) Conference Series, Vol. 9145, Society of Photo-Optical Instrumentation Engineers (SPIE) Conference Series, 22
- Berger, P., Newburgh, L. B., Amiri, M., et al. 2016, in Proc. SPIE, Vol. 9906, Society of Photo-Optical Instrumentation Engineers (SPIE) Conference Series, 99060D
- Burke-Spolaor, S., & Bannister, K. W. 2014, *ApJ*, 792, 19
- Caleb, M., Flynn, C., Bailes, M., et al. 2016, *MNRAS*, 458, 718
- Champion, D. J., Petroff, E., Kramer, M., et al. 2016, *MNRAS*, arXiv:1511.07746
- Chatterjee, S., Law, C. J., Wharton, R. S., et al. 2017, *ArXiv e-prints*, arXiv:1701.01098
- Chawla, P., Kaspi, V. M., Josephy, A., et al. 2017, *ArXiv e-prints*, arXiv:1701.07457
- Coenen, T., van Leeuwen, J., Hessels, J. W. T., et al. 2014, *A&A*, 570, A60
- Connor, L., Lin, H.-H., Masui, K., et al. 2016a, *MNRAS*, 460, 1054
- Connor, L., Sievers, J., & Pen, U.-L. 2016b, *MNRAS*, 458, L19
- Davis, G. 2012, PhD thesis, University of British Columbia, doi:http://dx.doi.org/10.14288/1.0072797.  
<https://open.library.ubc.ca/cIRcle/collections/24/items/1.0072797>
- Denman, N., Amiri, M., Bandura, K., et al. 2015, *ArXiv e-prints*, arXiv:1503.06202
- Falcke, H., & Rezzolla, L. 2014, *A&A*, 562, A137

- Karastergiou, A., Chennamangalam, J., Armour, W., et al. 2015, *MNRAS*, 452, 1254
- Kashiyama, K., Ioka, K., & Mészáros, P. 2013, *ApJL*, 776, L39
- Lorimer, D. R., Bailes, M., McLaughlin, M. A., Narkevic, D. J., & Crawford, F. 2007, *Science*, 318, 777
- Lyutikov, M., Burzawa, L., & Popov, S. B. 2016, *ArXiv e-prints*, arXiv:1603.02891
- Macquart, J.-P., & Johnston, S. 2015, *MNRAS*, 451, 3278
- Macquart, J.-P., Bailes, M., Bhat, N. D. R., et al. 2010, *PASA*, 27, 272
- Manchester, R. N., Hobbs, G. B., Teoh, A., & Hobbs, M. 2005, *AJ*, 129, 1993
- Mao, S., & Paczynski, B. 1992, *ApJL*, 388, L45
- Marcote, B., Paragi, Z., Hessels, J. W. T., et al. 2017, *ApJL*, 834, L8
- Masui, K., Lin, H.-H., Sievers, J., et al. 2015, *Nature*, 528, 523
- Metzger, B. D., Berger, E., & Margalit, B. 2017, *ArXiv e-prints*, arXiv:1701.02370
- Murase, K., Kashiyama, K., & Mészáros, P. 2016, *MNRAS*, 461, 1498
- Nava, L., Ghirlanda, G., Ghisellini, G., & Celotti, A. 2011, *MNRAS*, 415, 3153
- Newburgh, L. B., Addison, G. E., Amiri, M., et al. 2014, in *Proc. SPIE*, Vol. 9145, Ground-based and Airborne Telescopes V, 91454V
- Ng, C., Vanderlinde, K., Paradise, A., et al. 2017, *ArXiv e-prints*, arXiv:1702.04728
- Oppermann, N., Connor, L. D., & Pen, U.-L. 2016, *MNRAS*, 461, 984
- Petroff, E., Bailes, M., Barr, E. D., et al. 2015a, *MNRAS*, 447, 246
- Petroff, E., Keane, E. F., Barr, E. D., et al. 2015b, *MNRAS*, 451, 3933
- Petroff, E., Barr, E. D., Jameson, A., et al. 2016, *PASA*, 33, e045
- Piro, A. L. 2016, *ApJL*, 824, L32
- Ravi, V., Shannon, R. M., Bailes, M., et al. 2016, *Science*, 354, 1249
- Recnik, A., Bandura, K., Denman, N., et al. 2015, *ArXiv e-prints*, arXiv:1503.06189
- Romero, G. E., del Valle, M. V., & Vieyro, F. L. 2016, *PhRvD*, 93, 023001
- Schmidt, M. 1968, *ApJ*, 151, 393
- Scholz, P., Spitler, L. G., Hessels, J. W. T., et al. 2016, *ApJ*, 833, 177
- Shaw, J. R., Sigurdson, K., Sitwell, M., Stebbins, A., & Pen, U.-L. 2015, *PhRvD*, 91, 083514
- Siemion, A. P. V., Bower, G. C., Foster, G., et al. 2012, *ApJ*, 744, 109
- Spitler, L. G., Scholz, P., Hessels, J. W. T., et al. 2016, *Nature*, 531, 202
- Tendulkar, S. P., Bassa, C. G., Cordes, J. M., et al. 2017, *ApJL*, 834, L7
- Thornton, D., Stappers, B., Bailes, M., et al. 2013, *Science*, 341, 53
- Tingay, S. J., Trott, C. M., Wayth, R. B., et al. 2015, *AJ*, 150, 199
- van Leeuwen, J. 2014, in *The Third Hot-wiring the Transient Universe Workshop*, ed. P. R. Wozniak, M. J. Graham, A. A. Mahabal, & R. Seaman, 79–79
- Vedantham, H. K., Ravi, V., Hallinan, G., & Shannon, R. M. 2016, *ApJ*, 830, 75